Tunability of multiple ultraflat bands and effect of spin-orbit coupling in twisted bilayer transition metal dichalcogenides

Zhen Zhan [1], Yipei Zhang,[1] Pengfei Lv,[1] Hongxia Zhong,[1] Guodong Yu [1,2] Francisco Guinea,[3] José Ángel Silva-Guillén [1,*] and Shengjun Yuan [1,†]

[1]*Key Laboratory of Artificial Micro- and Nano-structures of Ministry of Education and School of Physics and Technology, Wuhan University, Wuhan 430072, China*
[2]*Institute for Molecules and Materials, Radboud University, Heijendaalseweg 135, NL-6525 AJ Nijmegen, The Netherlands*
[3]*Fundación IMDEA Nanociencia, C/Faraday 9, Campus Cantoblanco, E-28049 Madrid, Spain*

Ultraflat bands that have been theoretically and experimentally detected in a bunch of van der Waals stacked materials show some peculiar properties, for instance, highly localized electronic states and enhanced electron-electron interactions. In this Rapid Communication, using an accurate tight-binding model, we study the formation and evolution of ultraflat bands in transition metal dichalcogenides (TMDCs) under low rotation angles. We find that, unlike in twisted bilayer graphene, ultraflat bands exist in TMDCs for almost any small twist angles and their wave function becomes more localized when the rotation angle decreases. Lattice relaxation, pressure, and local deformation can tune the width of the flat bands, as well as their localization. Furthermore, we investigate the effect of spin-orbit coupling on the flat bands and discover spin/orbital/valley locking at the minimum of the conduction band at the K point of the Brillouin zone. Ultraflat bands found in TMDCs with a range of rotation angle below $7°$ may provide an ideal platform to study strongly correlated states.

Introduction. Stacked van der Waals layered systems provide an ideal platform to modulate the electronic properties of their parent materials via different degrees of freedom, for example, the rotation angle [1,2]. One of the most interesting phenomenon in these twisted two-dimensional (2D) materials is the formation of flat bands. Recently, it has been discovered that, in the so-called magic-angle twisted bilayer graphene, a flat band forms near the Fermi level and strongly correlated states, for instance, a Mott insulating behavior and unconventional superconductivity, arise from such a flat band [3,4]. This generated an intensive investigation on this matter in order to identify bilayer systems that present these kinds of electronic properties and that could be used as an ideal platform to study many-body interaction physics [5–8].

The engineering of quantum states of matter is an active area of experimental and theoretical research in modern condensed matter physics. In two-dimensional crystals and van der Waals materials, such controllable engineering can be realized by means of the rotation angle, pressure, strain, or local deformation [9,10]. For instance, the modification of the magic-angle value of twisted bilayer graphene has been realized by application of a uniaxial strain [11]. In fact, atomically thin 2D materials are particularly suited for strain engineering. For example, single-particle bound states can be created and confined by strain at the center of bubbles in monolayers of TMDCs [12]. A strain superlattice can lead to bands which describe a topological insulator [13]. As a designing parameter, interlayer coupling can be tuned by variable local stackings to tailor the electronic properties of van der Waals materials [14–16]. Recently, flat bands have been both theoretically predicted and experimentally observed in transition metal dichalcogenides (TMDCs) [8,17–27]. The question arises how other tuning parameters (for instance, the moiré effect, the pressure, local deformation, and the spin-orbit coupling) engineer ultraflat bands and their novel properties of twisted bilayer TMDCs.

In this Rapid Communication, we use an accurate *ab initio* tight-binding Hamiltonian [28,29] to investigate the engineering of ultraflat bands in twisted bilayer TMDCs with low rotation angles. The tight-binding propagation method is adopted to calculated the electronic properties of the moiré supercell, especially for samples with tiny rotation angles [30,31]. We construct twisted bilayer TMDCs by starting from a $2H$ stacking ($\theta = 0°$) and rotating the top layer with an angle θ with respect to the bottom layer around an atom site [29,32]. The moiré pattern has C_3 symmetry with the threefold rotation axis perpendicular to the TMDC plane. As illustrated in the Supplemental Material [32], in the supercell we can distinguish three different high-symmetry stackings (AB, $B^{S/S}$, and $B^{Mo/Mo}$). The band structure of monolayer transition metal dichalcogenides can be described by a tight-binding Hamiltonian consisting of 11 orbitals, the d orbitals from Mo and the p orbitals from the S [33–35]. The generalization to the bilayer case (including the twisted bilayer system) is done by adding an interlayer hopping term of the p orbitals of the chalcogen between adjacent layers to two single-layer Hamiltonians [28,29,33]. Tight-binding models are quite useful for the investigation of large-scale complicated systems and for the systematic study of the local strain effect on the electronic properties of 2D materials.

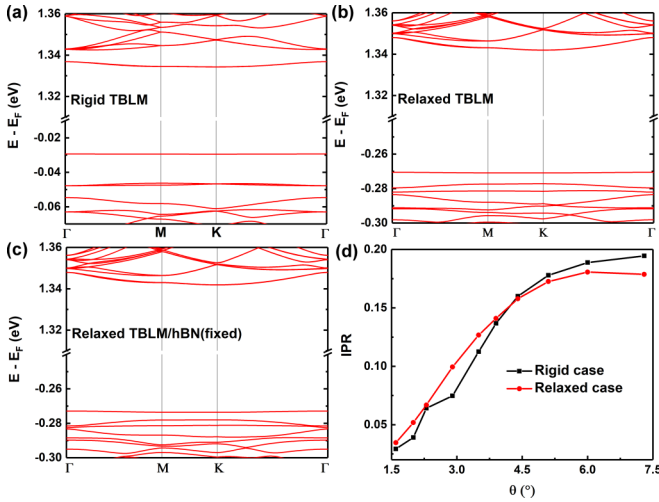*josilgui@gmail.com
†s.yuan@whu.edu.cn

FIG. 1. The band structure of (a) rigidly twisted bilayer MoS_2, (b) relaxed TBLM, and (c) relaxed TBLM/hBN with $\theta = 2.0°$. The hBN layer is fixed in a flat configuration. (d) Variation of the inverse participation ratio (IPR) with the rotation angle. Spin-orbit coupling is not included in the calculation.

Rotation angle. Via exact diagonalization of the *ab initio* tight-binding Hamiltonian of the twisted bilayer MoS_2 (TBLM), we carefully study the evolution of band structures under different rotation angles from $\theta = 7.3°$ to $\theta = 1.6°$. When the rotation angle approaches $0°$, for instance, for a rigidly twisted bilayer MoS_2 with $\theta = 2.0°$ [see Fig. 1(a)], multiple energy-separated ultraflat bands emerge at the valence band (VB) edge, which are localized at the $B^{S/S}$ region [18,19]. Moreover, an ultraflat band forms at the conduction band (CB) edge and its wave function is localized at the $B^{Mo/Mo}$ region [32]. These ultraflat bands resemble the quantized energy levels of bound states of a particle in a potential well, indicating that the electron suffers a strong and deep effective moiré potential [18,19]. The bandwidth (energy difference between the Γ and K points in the valence band edge) undergoes a drastic change from 30 meV to nearly zero as the rotation angle decreases from $7.3°$ to $1.6°$ [32]. Ultraflat bands also occur at the valence band edge of twisted bilayer $MoSe_2$, WS_2, and WSe_2 as well [32], which is consistent with a recent experimental result [21]. There are two reasons that can explain the flattening of bands: (i) The first is trivial—the growing size of the moiré unit cell shrinks the moiré Brillouin zone (MBZ). Since the MBZ is smaller than the original Brillouin zone (BZ), the energy bands simply fold into the MBZ and could cause band flattening. (ii) The evolution of the interlayer interaction due to the formation of a moiré structure can also cause band flattening while resulting in a nontrivial modulation of the electronic properties. It was discovered both theoretically and experimentally that in twisted bilayer systems, the electronic states of the flat bands are highly localized at the $B^{S/S}$ or $B^{Mo/Mo}$ high-symmetry stacking regions in real space, trapped by the effective periodic moiré potential and forming networks analogous to arrays of quantum dots [17–19].

Relaxation. In a real twisted bilayer system which is composed of various high-symmetry stackings, since the

stackings have different binding energies, the lattice structure spontaneously relaxes to achieve an energetically favorable structure [17]. In the reconstructed moiré supercell, different high-symmetry stacking patterns have different interlayer distances. Such a variation is expected to affect the electronic properties of the supercell. In order to study this effect we perform relaxations in two different realistic systems, a free-standing sample and another which is deposited on a hexagonal boron nitride (hBN) substrate. We perform the relaxations using the LAMMPS [36,37] package with the intralayer Stilliner-Weber (SW) potential [38] and the interlayer Lennard-Jones (LJ) potential [39]. Then, the interlayer hoppings are reconstructed according to the positions of the atoms. Our calculations show that the calculated TB band structure based on the relaxed structure agrees well with the density functional theory (DFT) result obtained from SIESTA [32,40–45]. As shown in Figs. 1(b) and 1(c), the first band in the valence band is still quite flat in the TBLM with $\theta = 2.0°$, whereas the energy separation from the other valence bands is reduced. Importantly, the spatial localization of the ultraflat bands changes from the $B^{S/S}$ site to the AB site [32]. The states are still localized at the AB site even if the atoms are kept fixed in plane [32]. Therefore, the underlying physical mechanism responsible for the formation of the ultraflat band in the valence band is a combination of the interlayer van der Waals interaction and the in-plane strain [18]. Moreover, a flat band with a larger bandwidth forms at the conduction band, which is still localized in the $B^{Mo/Mo}$ site.

To compare the localization of wave functions in the TBLM, we calculate the inverse participation ratio (IPR), which in a tight-binding model with N orbitals is defined as [46,47]

$$\text{IPR} = \sum_{i=1}^{N} |a_i^{\alpha}|^2 \Big/ \left(N \sum_{i=1}^{N} |a_i^{\alpha}|^4 \right), \quad (1)$$

where a_i^{α} is the amplitude for the eigenstate α at the site i. The evolution of the IPR of the states at K in the VB edge is plotted in Fig. 1(d). As the rotation angle becomes smaller, the IPR decreases monotonically, showing evidence of electron localization. The lattice relaxation has a different effect on the localization in the TBLM supercell depending on the rotation angle. That is, it makes the states more localized in large angle samples, whereas it weakens the localization for systems with small angles.

Compression. The possibility of modifying ultraflat bands and their associated correlated physics in twisted bilayer TMDCs by the application of uniaxial compression is investigated. In Fig. 1 we can see that, for TBLM with $\theta = 2.0°$, ultraflat bands emerge on both the CB and VB edges. Compression in the direction perpendicular to the bilayers is implemented in terms of $\sigma = 1 - (d'_{2H}/d_{2H})$, where d'_{2H} is the distance between repeating two-monolayer units and $d_{2H} = 12.29$ Å is the distance at zero compression.

If we pull apart the layers (negative compression), as shown in Fig. 2 isolated ultraflat bands near the CB and VB edges go deeper into the CB and VB, respectively and disappear, whereas the top VB ultraflat band is robust. More interestingly, as the positive compression increases, the layers
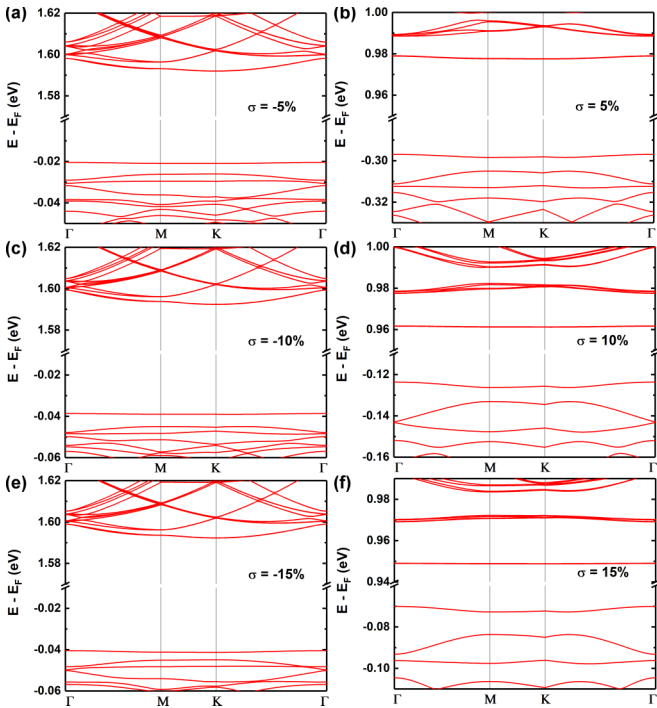
FIG. 2. The band structure (without SOC) of relaxed TBLM with $\theta = 2.0°$ under different vertical compressions.

FIG. 3. The band structure (without SOC) of 2° rigidly twisted bilayer MoS$_2$ with local deformation at (a) the B$^{S/S}$ region and (b) both the AB and B$^{S/S}$ regions. The insets are the side view of the atomic model along the direction of the three high-symmetry stackings (AB, B$^{Mo/Mo}$, and B$^{S/S}$). The local deformation is realized by implementing a Gaussian-type bubble at the B$^{S/S}$ or AB regions and with the center located at the B$^{S/S}$ or AB site, respectively. (c) The calculated local density of states mapping with energies of the CB and VB edges labeled in (b).

come closer and the effective interlayer coupling strength increases, which creates more energy-separated ultraflat bands in both CB and VB edges. The top flat band in the VB has a larger energy separation from other bands in the systems suffering a higher positive compression. Such multiple energy-separated ultraflat bands are similar to the DFT result in Ref. [18]. Compression does not change the localization of the ultraflat bands [32]. Moreover, a progressive closure of the band gap is obtained as the compression increases, which indicates that a metallization of twisted TMDCs may occur at compression larger than 15%. Such metallization could be investigated in an experimental setup with the application of pressure on TBLM higher than 56 GPa [32,48,49].

Local deformation. Specific strain textures can be produced in a system by applying an external strain, indenting with nanopillars patterned in a substrate, or stacking one layer on another lattice-mismatched layer [50–54]. Such deformation has a significant influence on the electronic properties of the system. For instance, spatially tailored pseudomagnetic fields were detected in graphene-based devices [54]. How the local deformation will affect the ultraflat bands in twisted bilayer TMDCs is still unclear. In this part, a Gaussian-type bubble with a radius $R = 26$ Å is created at a high-symmetry stacking region (AB or B$^{S/S}$) of the TBLM with $\theta = 2°$. The in-plane separation between the high-symmetry stacking sites is 90 Å. The center of the bubble is located at either the AB or B$^{S/S}$ site (see Fig. 3) and the maximum out-of-plane displacements h_{max} at both AB and B$^{S/S}$ are $0.05d_{2H}$. The bubble has a height-over-radius ratio $h_{max}/R = 0.04$, in which the in-plane lattice deformation can be neglected safely. We only concentrate on the effect of interlayer couplings and, for simplicity, we will keep the same in-plane hopping value that
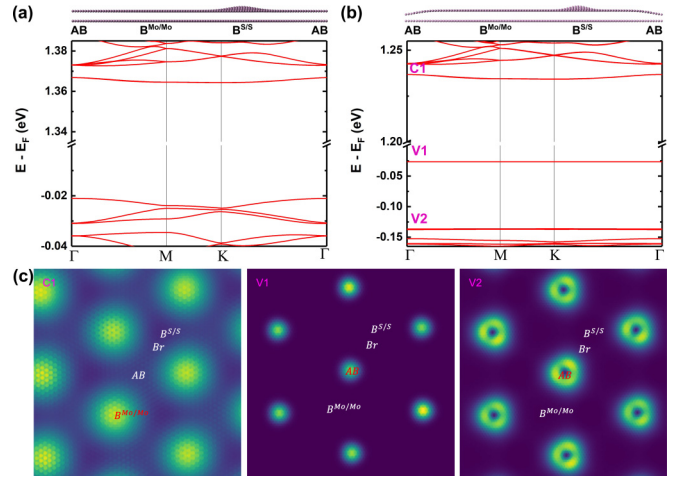
is independent of the local deformation and also do not relax the system.

In Fig. 3(a), the multiple ultraflat bands that localize at the B$^{S/S}$ region are destroyed upon the presence of the bubble. When the interlayer distance increases inside the bubble, the interlayer interaction decreases, which kills the ultraflat band in the VB edge. After, we can generate a concave bubble with the same shape at the AB region [see the top of Fig. 3(b)]. Interestingly, as seen in Fig. 3(b), multiple energy-separated ultraflat bands form again in the VB edges. When the height of the bubble increases, more ultraflat bands appear in the VB [32]. Different from the moiré pattern without local deformation, as shown in Fig. 3(c), the new ultraflat band states are localized at the AB region. Differently, the local deformations in both AB and B$^{S/S}$ regions make minor changes to the ultraflat band on the CB edge and its localization. All in all, the local deformation is remarkably efficient to tune the ultraflat band as well as its localization.

Spin-orbit coupling. Transition metal dichalcogenides, in particular, single-layer TMDCs, have strong spin-orbit coupling (SOC) and broken inversion symmetry which lead to opposite spin polarizations on different valleys. The locked spin and valley pseudospin gives rise to rich valley physics and makes TMDCs promising materials for next generation optoelectronic applications [55,56]. For non-twisted bilayer TMDCs, no valley-dependent spin polarization is detected due to the presence of inversion symmetry. Such symmetry can be broken by applying an external electric field perpendicular to the bilayer [57]. In this section, we investigate the effect of SOC on the band structure of twisted bilayer MoS$_2$, where the mirror symmetry is broken by the rotation angle. In the tight-binding model, the effect of SOC is well captured by doubling the orbitals and including an on-site
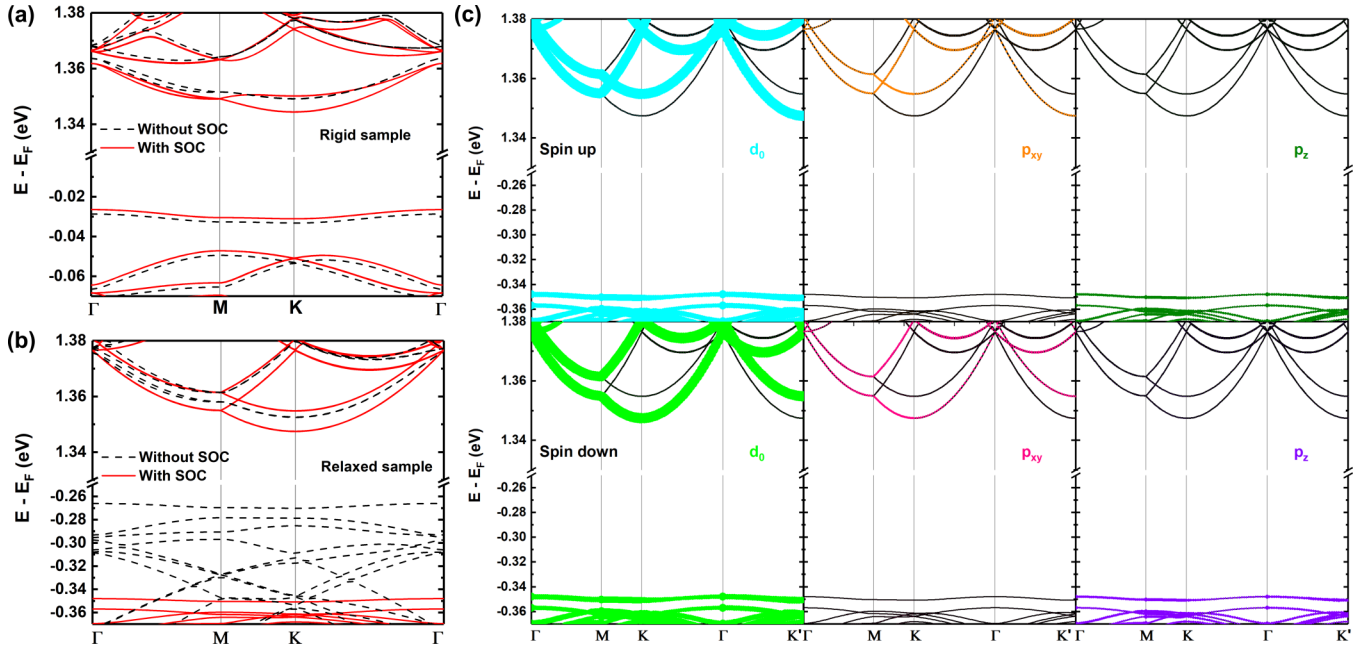
FIG. 4. The band structures with and without SOC of twisted bilayer MoS$_2$ with rotation angles $\theta = 3.5°$ in the (a) rigid case and (b) relaxed case. (c) The band structure (with SOC) and orbital weight of the relaxed TBLM with 3.5°. The thickness of the bands representing the orbital weight with the d character ($d_2 = d_{x^2-y^2}$, d_{xy}, $d_1 = d_{xz}$, d_{yz}, $d_0 = d_{3z^2-r^2}$) refers to the Mo atom $4d$ orbitals and the p character ($p_{xy} = p_x$, p_y) refers to S atom $2p$ orbitals. The orbital weights of d_2 and d_1 are not shown here. The sum orbital weight of d_0, p_{xy}, and p_z is up to 97%.

term $\sum_\alpha \lambda_\alpha \mathbf{L} \cdot \mathbf{S}$ in the Hamiltonian, where subscript α stands for the type of atom [28,34,58]. The band structures with (red solid line) and without spin-orbit coupling (dashed black line) are shown in Figs. 4(a) and 4(b) for unrelaxed and relaxed samples with $\theta = 3.5°$, respectively.

From these figures we observe that, upon rotation, as a consequence of breaking the mirror symmetry, spin degeneracies are lifted along the Γ-K-M path, but the time reversal invariant points Γ and M remain spin degenerate. Furthermore, opposite to the single-layer case, the effect of SOC is more significant in the conduction band for the twisted bilayer system. In the monolayer, the conduction band edge at the K point has a d_0 character [33]. For these states, $\langle \mathbf{L} \cdot \mathbf{S} \rangle = 0$, and the effect of the spin orbit requires second-order processes in perturbation theory [59]. The states at the K point of MoS$_2$ have a contribution to the flat bands studied here [32]. These states have a significant S p_x, p_y character, where the splitting due to the spin-orbit coupling is a first-order process. Meanwhile, at the conduction band edge, the K valley has the largest spin splitting and shrinks when the rotation angle decreases. Such shrinkage in the relaxed samples is smoother than in the rigid case [32]. Focusing on the valence band edges, we find that the ultraflat band at the valence band edge is doubly spin degenerate in the whole BZ. As shown in Fig. 4, there is no spin splitting at the VB edge. That is highly consistent with the DFT result [60].

We further calculate the orbital weight for the band structure of TBLM with $\theta = 3.5°$. States at the bottom of the conduction band mainly consist of p_{xy} and d_0 orbitals, and the two inequivalent valleys are spin locked. That is, the spin-up states at valley K are degenerate with spin-down states at valley K', and vice versa. That is different from the monolayer case where the Q point has the largest band splitting

with spin polarization. The ultraflat band at the valence band edge is mainly composed of d_0 and p_z orbitals and is indeed spin degenerate. These bands are located away from the K point of the MoS$_2$ non-twisted bilayer (consists of d_2 and p_{xy} orbitals), and thus show a reduced SOC splitting [32]. In the CB an ultraflat band is formed and its localization is at the $B^{Mo/Mo}$ region. Such a band is almost composed solely by d_0 orbitals while it has a finite contribution from p_{xy} orbitals. This indicates a different origin of the ultraflat bands near the conduction band. The electronic states at the conduction band edge are nearly decoupled from each other for two different layers, as there is little interlayer interaction for $B^{Mo/Mo}$ stacking. That explains why the relaxation and local deformation do not change the localization of the VB edge state. This property might allow independent manipulation of electronic states in the conduction band minimum for the two different layers.

Conclusions. We have studied the evolution of the band structure of twisted bilayer MoS$_2$. We found that as the rotation angle decreases, the bandwidth decreases monotonically and the flat-band wave functions become more localized as well. When the rotation angle is below a certain value, flat bands start to emerge at the valence band and multiple energy-separated flat bands form at the conduction band. Furthermore, compression and mechanical strain are effective methods to tune the flat bands and their localization in real space. Finally, we analyzed the orbital composition near the band edge in the presence of SOC. We show that the states in the conduction band edge are spin polarized, and the polarization is opposite in K and K'. Therefore, the effect of spin-orbit coupling should be taken into account when developing simpler models for these kinds of systems. The physical mechanisms responsible for the formation of flat

bands in the CB and VB are different. We also found that the electronic states at the conduction band edge are independent for the two layers according to their orbital contribution. Note that if one wishes to tune the flat band significantly using the rotation angle, it is better to suppress the structural relaxation in the system. Ultraflat bands are also detected in other twisted bilayer TMDCs, for instance, $MoSe_2$, WS_2, and WSe_2 [32], which indicates that twisted TMDCs could be used as an ideal platform for the understanding of correlated behaviors.

[1] R. Bistritzer and A. H. MacDonald, Proc. Natl. Acad. Sci. U.S.A. Sci. **108**, 12233 (2011).

[2] I. Brihuega, P. Mallet, H. González-Herrero, G. Trambly de Laissardière, M. M. Ugeda, L. Magaud, J. M. Gómez-Rodríguez, F. Ynduráin, and J.-Y. Veuillen, Phys. Rev. Lett. **109**, 196802 (2012).

[3] Y. Cao, V. Fatemi, A. Demir, S. Fang, S. L. Tomarken, J. Y. Luo, J. D. Sanchez-Yamagishi, K. Watanabe, T. Taniguchi, E. Kaxiras *et al.*, Nature (London) **556**, 80 (2018).

[4] Y. Cao, V. Fatemi, S. Fang, K. Watanabe, T. Taniguchi, E. Kaxiras, and P. Jarillo-Herrero, Nature (London) **556**, 43 (2018).

[5] A. Kerelsky, L. J. McGilly, D. M. Kennes, L. Xian, M. Yankowitz, S. Chen, K. Watanabe, T. Taniguchi, J. Hone, C. Dean *et al.*, Nature (London) **572**, 95 (2019).

[6] Y. Xie, B. Lian, B. Jäck, X. Liu, C.-L. Chiu, K. Watanabe, T. Taniguchi, B. A. Bernevig, and A. Yazdani, Nature (London) **572**, 101 (2019).

[7] T. M. R. Wolf, J. L. Lado, G. Blatter, and O. Zilberberg, Phys. Rev. Lett. **123**, 096802 (2019).

[8] F. Wu, T. Lovorn, E. Tutuc, and A. H. MacDonald, Phys. Rev. Lett. **121**, 026402 (2018).

[9] R. Roldán, L. Chirolli, E. Prada, J. A. Silva-Guillén, P. San-Jose, and F. Guinea, Chem. Soc. Rev. **46**, 4387 (2017).

[10] B. Amorim, A. Cortijo, F. De Juan, A. Grushin, F. Guinea, A. Gutiérrez-Rubio, H. Ochoa, V. Parente, R. Roldán, P. San-Jose *et al.*, Phys. Rep. **617**, 1 (2016).

[11] S. Carr, S. Fang, P. Jarillo-Herrero, and E. Kaxiras, Phys. Rev. B **98**, 085144 (2018).

[12] L. Chirolli, E. Prada, F. Guinea, R. Roldán, and P. San-Jose, 2D Mater. **6**, 025010 (2019).

[13] M. A. Cazalilla, H. Ochoa, and F. Guinea, Phys. Rev. Lett. **113**, 077201 (2014).

[14] C. Zhang, C.-P. Chuu, X. Ren, M.-Y. Li, L.-J. Li, C. Jin, M.-Y. Chou, and C.-K. Shih, Science Adv. **3**, e1601459 (2017).

[15] K. Liu, L. Zhang, T. Cao, C. Jin, D. Qiu, Q. Zhou, A. Zettl, P. Yang, S. G. Louie, and F. Wang, Nat. Commun. **5**, 4966 (2014).

[16] A. A. Puretzky, L. Liang, X. Li, K. Xiao, B. G. Sumpter, V. Meunier, and D. B. Geohegan, ACS Nano **10**, 2736 (2016).

[17] M. H. Naik and M. Jain, Phys. Rev. Lett. **121**, 266401 (2018).

[18] M. H. Naik, S. Kundu, I. Maity, and M. Jain, Phys. Rev. B **102**, 075413 (2020).

[19] M. Fleischmann, R. Gupta, S. Sharma, and S. Shallcross, arXiv:1901.04679.

[20] S. Venkateswarlu, A. Honecker, and G. Trambly de Laissardière, Phys. Rev. B **102**, 081103(R) (2020).

[21] Z. Zhang, Y. Wang, K. Watanabe, T. Taniguchi, K. Ueno, E. Tutuc, and B. J. LeRoy, Nat. Phys. **16**, 1093 (2020).

[22] L. Wang, E.-M. Shih, A. Ghiotto, L. Xian, D. A. Rhodes, C. Tan, M. Claassen, D. M. Kennes, Y. Bai, B. Kim *et al.*, Nat. Mater. **19**, 861 (2020).

[23] F. Wu, T. Lovorn, E. Tutuc, I. Martin, and A. H. MacDonald, Phys. Rev. Lett. **122**, 086402 (2019).

[24] C. Jin, E. C. Regan, A. Yan, M. I. B. Utama, D. Wang, S. Zhao, Y. Qin, S. Yang, Z. Zheng, S. Shi *et al.*, Nature (London) **567**, 76 (2019).

[25] E. C. Regan, D. Wang, C. Jin, M. I. B. Utama, B. Gao, X. Wei, S. Zhao, W. Zhao, Z. Zhang, K. Yumigeta *et al.*, Nature (London) **579**, 359 (2020).

[26] J. Sung, Y. Zhou, G. Scuri, V. Zólyomi, T. I. Andersen, H. Yoo, D. S. Wild, A. Y. Joe, R. J. Gelly, H. Heo *et al.*, Nat. Nanotechnol. **15**, 750 (2020).

[27] Y. Tang, L. Li, T. Li, Y. Xu, S. Liu, K. Barmak, K. Watanabe, T. Taniguchi, A. H. MacDonald, J. Shan, and K. F. Mak, Nature (London) **579**, 353 (2020).

[28] S. Fang, R. Kuate Defo, S. N. Shirodkar, S. Lieu, G. A. Tritsaris, and E. Kaxiras, Phys. Rev. B **92**, 205108 (2015).

[29] Y. Zhang, Z. Zhan, F. Guinea, J. Á. Silva-Guillén, and Y. Shengjun, arXiv:2005.13879.

[30] S. Yuan, H. De Raedt, and M. I. Katsnelson, Phys. Rev. B **82**, 115448 (2010).

[31] H. Shi, Z. Zhan, Z. Qi, K. Huang, E. van Veen, J. Á. Silva-Guillén, R. Zhang, P. Li, K. Xie, H. Ji *et al.*, Nat. Commun. **11**, 371 (2020).

[32] See Supplemental Material at http://link.aps.org/supplemental/10.1103/PhysRevB.102.241106 for details regarding the tight-binding model, structural relaxation, localization of the wave functions of the ultraflat bands, the charge density, the effect of the local deformation, the effect of the spin-orbit coupling, the band structure of $MoSe_2$, WS_2, and WSe_2, and the computational details.

[33] E. Cappelluti, R. Roldán, J. A. Silva-Guillén, P. Ordejón, and F. Guinea, Phys. Rev. B **88**, 075409 (2013).

[34] R. Roldán, M. P. López-Sancho, F. Guinea, E. Cappelluti, J. A. Silva-Guillén, and P. Ordejón, 2D Mater. **1**, 034003 (2014).

[35] R. Roldán, J. A. Silva-Guillén, M. P. López-Sancho, F. Guinea, E. Cappelluti, and P. Ordejón, Ann. Phys. **526**, 347 (2014).

[36] S. Plimpton, J. Comput. Phys. **117**, 1 (1995).

[37] LAMMPS website, http://lammps.sandia.gov.

[38] J.-W. Jiang, Nanotechnology **26**, 315706 (2015).

[39] A. K. Rappé, C. J. Casewit, K. Colwell, W. A. Goddard III, and W. M. Skiff, J. Am. Chem. Soc. **114**, 10024 (1992).

[40] J. M. Soler, E. Artacho, J. D. Gale, A. García, J. Junquera, P. Ordejón, and D. Sánchez-Portal, J. Phys.: Condens. Matter **14**, 2745 (2002).

[41] E. Artacho, E. Anglada, O. Diéguez, J. D. Gale, A. García, J. Junquera, R. M. Martin, P. Ordejón, J. M. Pruneda, D. Sánchez-Portal *et al.*, J. Phys.: Condens. Matter **20**, 064208 (2008).

[42] J. P. Perdew, K. Burke, and M. Ernzerhof, Phys. Rev. Lett. **77**, 3865 (1996).

[43] E. Artacho, D. Sánchez-Portal, P. Ordejón, A. Garcia, and J. M. Soler, Phys. Status Solidi B **215**, 809 (1999).

[44] S. Grimme, J. Comput. Chem. **27**, 1787 (2006).

[45] R. Cuadrado and J. Cerdá, J. Phys.: Condens. Matter **24**, 086005 (2012).

[46] T. Odagaki and D. Nguyen, Phys. Rev. B **33**, 2184 (1986).

[47] H. Huang and F. Liu, Phys. Rev. B **100**, 085119 (2019).

[48] N. Bandaru, R. S. Kumar, D. Sneed, O. Tschauner, J. Baker, D. Antonio, S.-N. Luo, T. Hartmann, Y. Zhao, and R. Venkat, J. Phys. Chem. C **118**, 3230 (2014).

[49] Z. Zhao, H. Zhang, H. Yuan, S. Wang, Y. Lin, Q. Zeng, G. Xu, Z. Liu, G. Solanki, K. Patel *et al.*, Nat. Commun. **6**, 7312 (2015).

[50] F. Guinea, M. Katsnelson, and A. Geim, Nat. Phys. **6**, 30 (2010).

[51] A. Branny, S. Kumar, R. Proux, and B. D. Gerardot, Nat. Commun. **8**, 15053 (2017).

[52] A. Reserbat-Plantey, D. Kalita, Z. Han, L. Ferlazzo, S. Autier-Laurent, C. Komatsu, C. Li, R. Weil, A. Ralko, L. Marty *et al.*, Nano Lett. **14**, 5044 (2014).

[53] H. Li, A. W. Contryman, X. Qian, S. M. Ardakani, Y. Gong, X. Wang, J. M. Weisse, C. H. Lee, J. Zhao, P. M. Ajayan *et al.*, Nat. Commun. **6**, 7381 (2015).

[54] Y. Liu, J. Rodrigues, Y. Z. Luo, L. Li, A. Carvalho, M. Yang, E. Laksono, J. Lu, Y. Bao, H. Xu *et al.*, Nat. Nanotechnol. **13**, 828 (2018).

[55] R. Suzuki, M. Sakano, Y. Zhang, R. Akashi, D. Morikawa, A. Harasawa, K. Yaji, K. Kuroda, K. Miyamoto, T. Okuda *et al.*, Nat. Nanotechnol. **9**, 611 (2014).

[56] G. Scuri, T. I. Andersen, Y. Zhou, D. S. Wild, J. Sung, R. J. Gelly, D. Bérubé, H. Heo, L. Shao, A. Y. Joe *et al.*, Phys. Rev. Lett. **124**, 217403 (2020).

[57] S. Wu, J. S. Ross, G.-B. Liu, G. Aivazian, A. Jones, Z. Fei, W. Zhu, D. Xiao, W. Yao, D. Cobden *et al.*, Nat. Phys. **9**, 149 (2013).

[58] J. Silva-Guillén, P. San-Jose, and R. Roldán, Appl. Sci. **6**, 284 (2016).

[59] H. Ochoa and R. Roldán, Phys. Rev. B **87**, 245421 (2013).

[60] P. Kumari, J. Chatterjee, and P. Mahadevan, Phys. Rev. B **101**, 045432 (2020).